GSA Data Repository 2016064

Isotopic evidence for iron mobility during subduction

B. Debret[1,2*], M.-A. Millet[1], M.-L. Pons[1,2], P. Bouilhol[1], E. Inglis[1], and H. Williams[1,2]
[1]*Department of Earth Sciences, Durham University, Durham DH1 3LE, U.K.*
[2]*Department of Earth Sciences, The University of Cambridge, Downing Street, Cambridge CB2 3EQ, U.K.*
*ba.debret@gmail.com

GEOLOGICAL SETTING

Our study focuses on the Piemont zone of the south-western Alps where ophiolitic units were metamorphosed and juxtaposed during alpine subduction and collision in Late Cretaceous to Tertiary (e.g. Tricart, 1984). We have sampled a serpentinite suite from 5 meta-ophiolites that record metamorphic conditions ranging from greenschist to eclogite facies (see Debret et al., 2014 for more detailed about this sample suite). The Chenaillet ophiolite is located in the external Piemont zone, 6km west of Briançon (Fig. DR1). It is a thin tectonic nappe resting upon the Queyras Schistes Lustrés complex (Caby, 1995). It is composed of metagabbroic pods and serpentinites recording greenschist facies conditions (Mevel et al., 1978). The Queyras Schistes Lustrés complex is composed of metamorphosed Mesozoic oceanic sediments, strongly deformed during alpine subduction (Tricart and Schwartz, 2006). The complex encloses boudinaged ophiolite units composed of serpentinites, metagabbros and metabasalts from meter to kilometer size, and records blueschist facies P-T conditions (Schwartz et al., 2013). The Monte Maggiore ophiolite is located in the northern end of the Cap Corse, Northern Corsica (Fig. DR1). It is an ultramafic body of ~4 km^2 surrounded by eclogitized continental units. The massif is composed of slightly serpentinized peridotites, serpentinites and metagabbros recording blueschist facies conditions (e.g. Vitale-Brovarone et al., 2013). The Monviso meta-ophiolite is located in the extreme East of the Queyras Schistes Lustrés complex (Fig. DR1). This ultramafic body is composed of kilometric lenses of metabasites embedded in highly deformed serpentinites recording eclogite facies P-T conditions (Schwartz et al., 2001). The Lanzo massif is an eclogitized ultramafic body of 150 km2 bounded by the sediments of the Po plain to the East and South, meta-ophiolites and the Schistes Lustrés unit in the West, and by the HP metamorphic continental unit of Sesia in the North (Pelletier and Müntener, 2006).

MAJOR ELEMENTS AND $Fe^{3+}/\Sigma Fe$ DETERMINATION

Major element concentrations were determined by ICP-AES at the Laboratoire Magmas et Volcans of Clermont-Ferrand (France) following procedures described in Debret et al. (2014a). Concentrations were calibrated against the DR-N basaltic glass (Govindaraju, 1994). Precision on samples were determined by repeated analyses of the reference basalt BHVO. The reproducibility is better than 5% for all measured elements. Additional Fe^{2+} analyses of bulk rock samples were performed at the SARM-CRPG (Nancy, France). These analyses were done by automatic titration at the equivalent point with potassium dichromate after dissolution of the sample in a HF/H_2SO_4 mixture, in the presence of H_3BO_3 and H_3PO_4

(Andreani et al., 2013). Subsequently $Fe^{3+}/\Sigma Fe$ ratios were calculated from the measured Fe_2O_{3total} and Fe^{2+}Total values (e.g. Andreani et al., 2013). The method has been tested by Debret et al. (2015), who were able to match measured bulk $Fe^{3+}/\Sigma Fe$ ratios with those recalculated from µ-XANES measurements of serpentine minerals (see Debret et al., 2014 and 2015 for more details on the method including standard ran in the XANES sessions, calibration and precision).

TRACE ELEMENTS

Trace element concentrations (Li, Sc, Ti, V, Co, Ni, Cu, Zn, As, Rb, Sr, Y, Zr, Nb, Cd, Sb, Cs, Ba, Rare Earth Elements (REE), Hf, Ta, Pb, Th, and U) are from Debret et al. (2013), Lafay et al. (2013) and this study (Table DR2). In this study, they were analysed at the National Oceanography Centre, Southampton using a Thermo X-Series Quadrupole ICP-MS. 10 mg of powdered sample were digested by addition of concentrated hydrofluoric and nitric acids. These solutions were then dried down and the reside dissolved in 2% HNO_3, which was spiked with 10ng/mL In and Re for use as an internal correction. The external precision and accuracy of the analyses were assessed by measuring as unknown three rock standards: BHVO and BIR-1 basalts and JA-2 peridotite. Our results show good agreement between measured values and expected values for international standards, and external reproducibility is within 0–5% for Sc, Ti, V, Ni, Cu, As, Rb, Sr, Y, Cd, Sb, Ba, La, Ce, Nd, Sm, Eu, Gd, Tb, Ho, Tm, Lu, Li, Co, Pr, Dy, Er, and Yb and within 10–30% for Cs, Hf, Nb, Ta, Pb, Th, U and Zr.

The Western Alps serpentinites have relatively uniform major element compositions that overlap with those of abyssal peridotites (Bodinier and Godard, 2013). Rare earth element (REE) concentration patterns of Western Alps SSP and Liz-serpentinite vary according to rock type, and range from lherzolite- to dunitic- like patterns. The lherzolite like pattern is characterized by depletion in light rare earth elements ($Ce_N/Yb_N \sim 0.1$; N: C1-chondrites normalized; LREE) and a flat medium and heavy rare earth element (M-HREE) segment ($Gd_N/Yb_N \sim 1$). The dunite-like pattern is concave and characterized by an enrichment in HREE relative to MREE ($Gd_N/Yb_N \sim 0.6$). The slightly serpentinized peridotites (SSP) display both positive and negative Eu anomalies, which probably reflect melt/rock interaction processes (Bodinier and Godard, 2013). Compared to the SSP, the Liz- and Atg/Liz- serpentinites can display enrichment in LREE relative to MREE and/or a negative anomaly in Ce relative to neighbouring elements reflecting seawater/rock interactions (Rouméjon et al., 2015) and the highest LREE mobility relative to M-HREE during sea floor serpentinization process (Paulick et al., 2006). During subduction, the prograde crystallization of lizardite and antigorite do not fractionate REE composition significantly, such that even highly metamorphosed serpentinites retain their protolith REE patterns (Debret et al., 2013). Atg- and Atg/Ol- serpentinites display similar patterns to lherzolites, which are characterized by depletion in LREE relative to M-HREE with the exception of two samples (Vis1F and Vis5b) which display U-shaped patterns.

Fe ISOTOPE ANALYSES

Iron isotope analyses were performed by multiple-collector inductively coupled plasma mass spectrometry (MC-ICPMS; Thermo Neptune Plus) at Durham University, utilizing a ^{57}Fe–^{58}Fe double spike (Millet et al., 2012) and/or by simple standard bracketing (Williams et al., 2005, Hibbert et al., 2012, Williams and Bizimis, 2014; Table DR1) to correct for instrumental mass bias. Both methods give

results within analytical error (Table DR1, Fig. DR3). Dissolution, iron purification and isotopic analyses were undertaken at Durham University using established procedures (Hibbert et al., 2012, Williams and Bizimis, 2014). In the case of double-spike analyses, solutions consisted of a mixture of 1.5 ppm Fe of 0.75 ppm sample and 0.75 ppm double spike in 0.1 M HNO_3, whereas for sample-standard bracketing they consisted of 2 ppm natural Fe in 0.1 M HNO_3. The standard Fe beam intensities typically varied between 25 and 35V ^{56}Fe for a standard $10^{-11}\Omega$ resistor. Mass dependence, long-term reproducibility and accuracy were evaluated by analysis of an in-house FeCl salt standard ($\delta^{56}Fe = -0.71 \pm 0.05$ ‰; $\delta^{57}Fe = -1.05 \pm 0.09$ ‰ 2sd, n =67) previously analysed in other studies (Williams et al., 2005, 2014; Weyer and Ionov, 2007; Millet et al., 2012). The USGS standards BIR-1 (Icelandic basalt) were also analysed over the course of this study. The mean Fe isotope composition of this standard is: $\delta^{56}Fe = 0.05 \pm 0.06$ ‰; $\delta^{57}Fe = 0.07 \pm 0.05$ ‰ (2sd, n = 4).

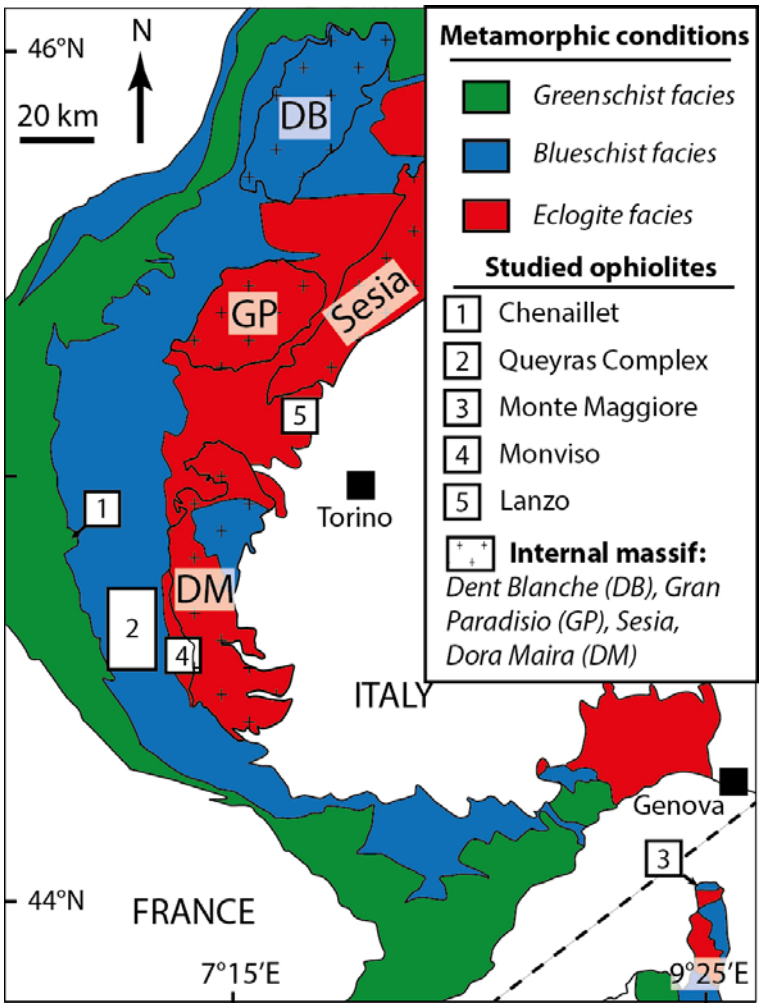

Figure DR1. Simplified metamorphic map of the Western Alps showing the spatial distribution of the studied ultramafic ophiolites (numbered white squares).

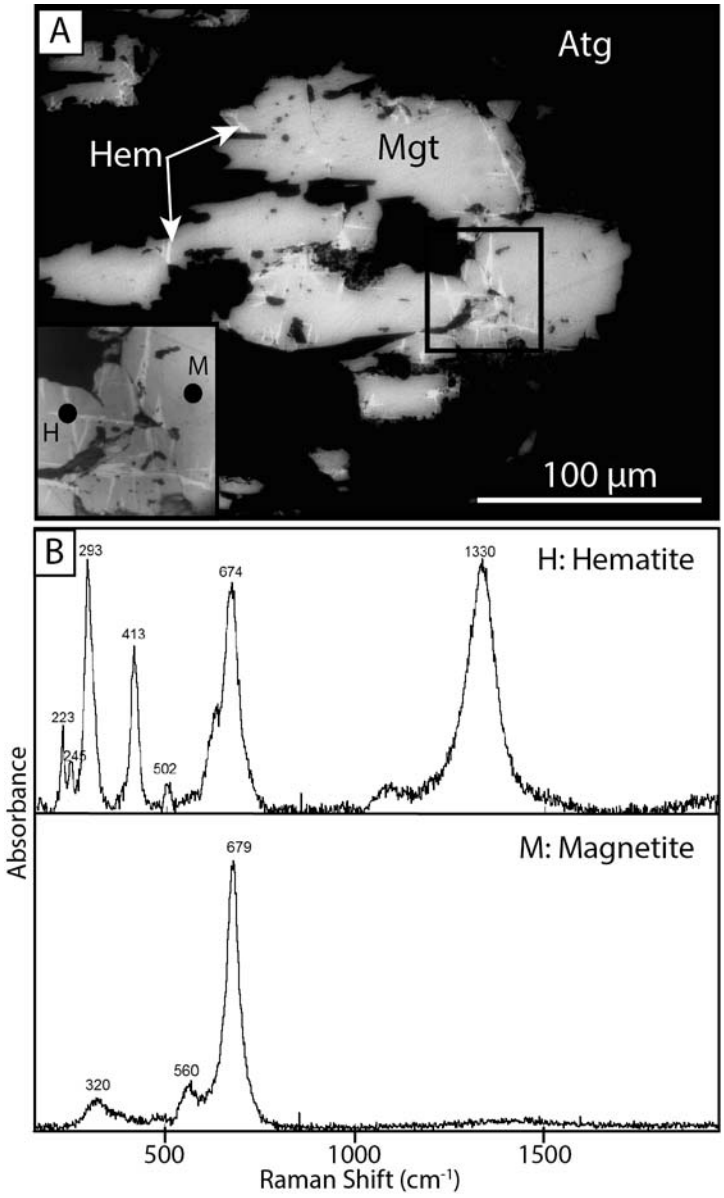

Figure DR2. A microphotograph of an Atg-serpentinite displaying magnetite grains containing white needles of hematite. The box displays a zoom of hematite needles with location of Raman analyses. Raman analyses of the white needles are characterized by four peaks at 223, 293, 413, and 1330 cm^{-1} corresponding to hematite. The Raman spectrum of magnetite is characterized by three peaks at 320, 560 and 679 cm^{-1}.

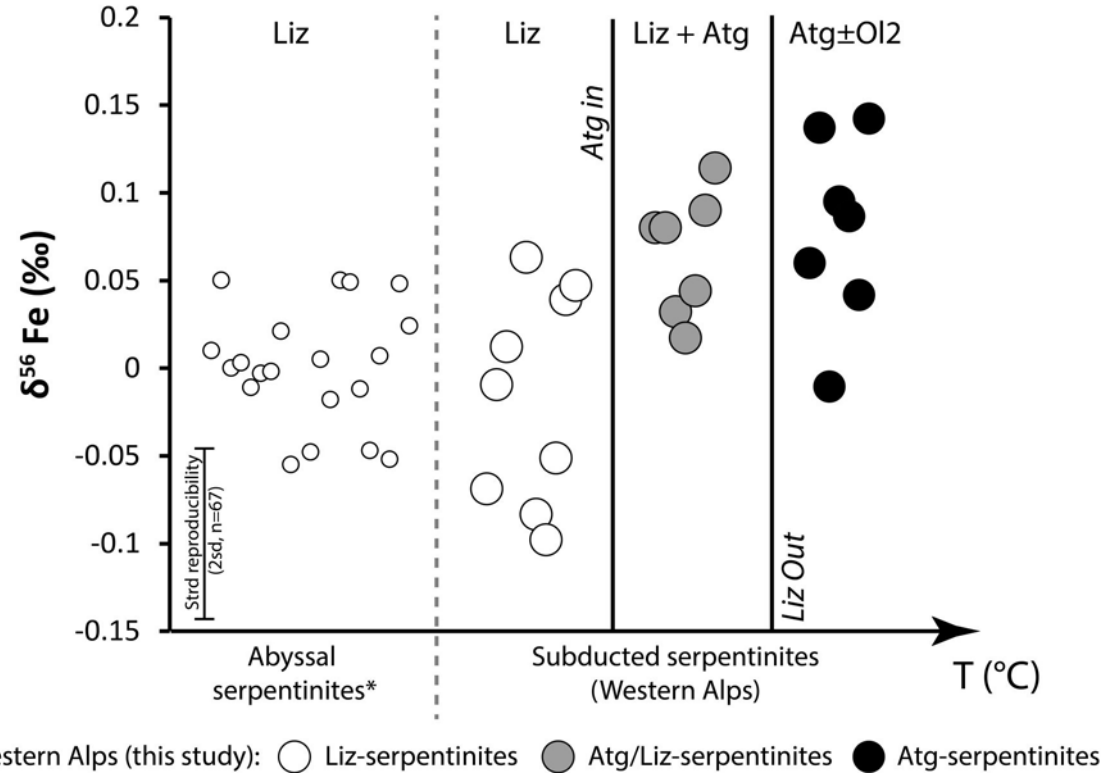

Figure DR3. Iron isotope composition of abyssal serpentinites (South West Indian Ridge and Gakkel ridge) and serpentinites from Western Alps ophiolites. Abyssal serpentinite values are from Craddock et al. (2013, non-weathered rocks). T-test indicates that the Liz-serpentinites and Atg/Liz-serpentinites are significantly different from each other at the 90% confidence interval (t = -3.05, d.f. = 14).

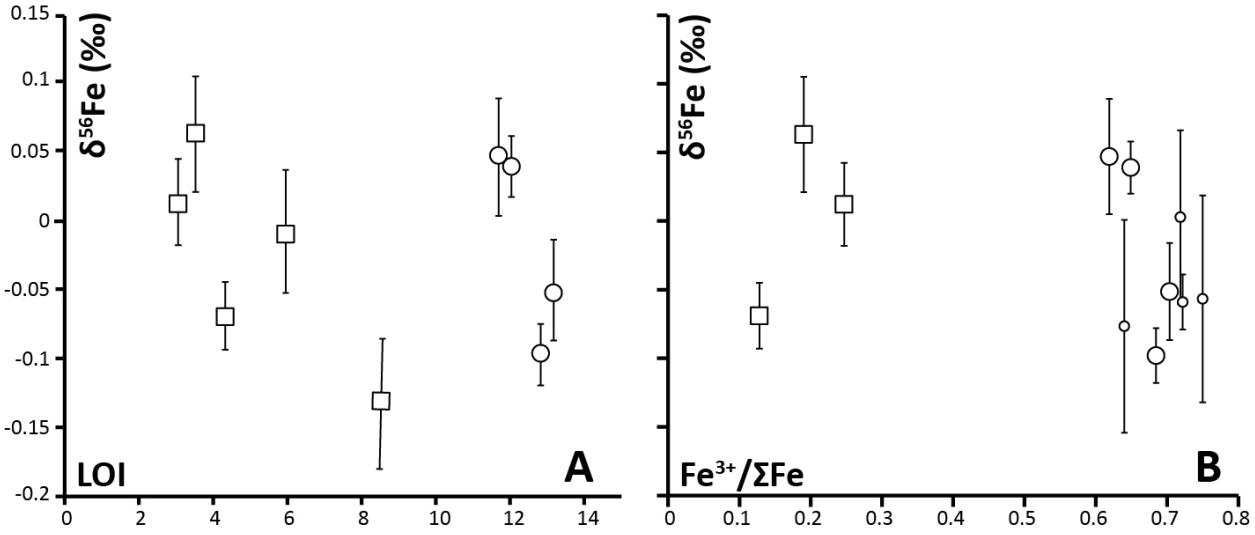

Figure DR4. Evolution of $\delta^{56}Fe$ as a function of peridotite serpentinization degree. Iron isotope composition ($\delta^{56}Fe$) of alpine SSP (white squares) and Liz-serpentinites (white circles) versus serpentinization degree proxies (A: Loss on ignition; B**:** $Fe^{3+}/\Sigma Fe$). Small circles correspond to abyssal serpentinites (Gakkel Ridge samples). Both plots show that there is no variation of iron isotopes in peridotite during serpentinization process.

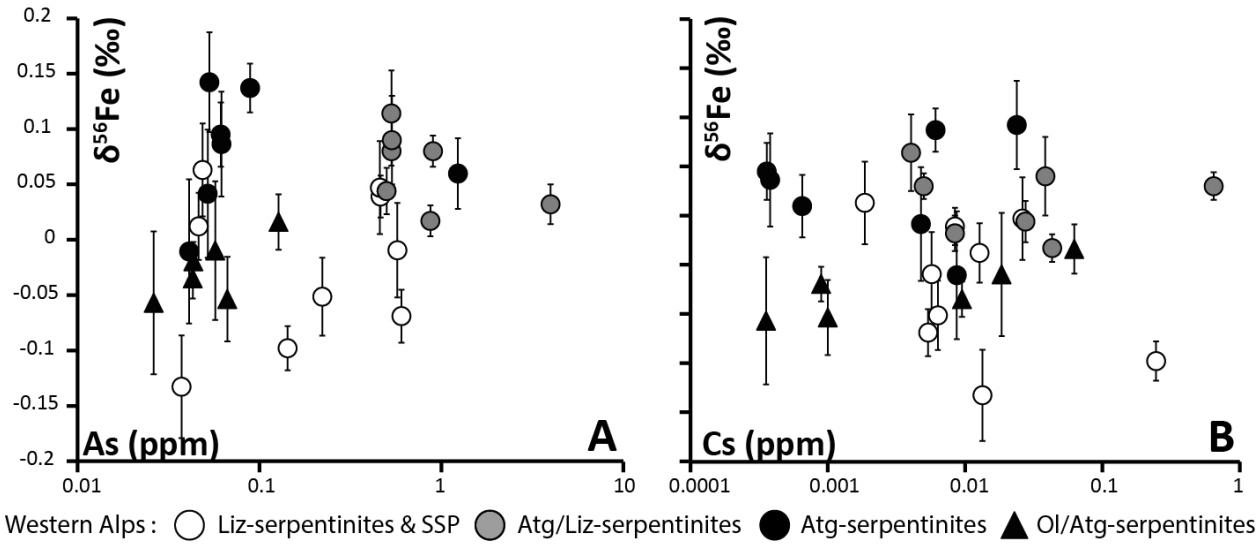

Figure DR5. Plot of δ^{56}Fe versus elemental tracers of sediment/serpentinite interactions. Both plots show that there is no correlation between both parameters showing that addition or release of Fe by sediment/serpentinite interactions is unlikely.

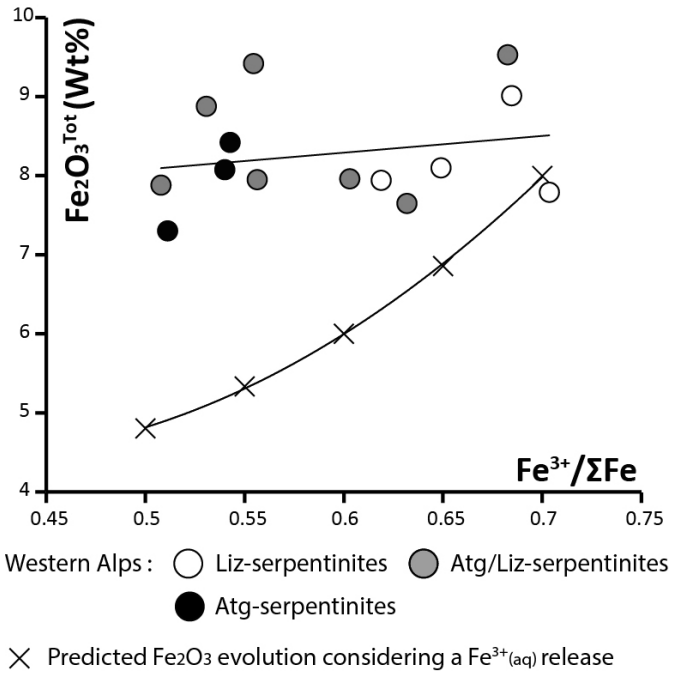

Figure DR6: Plot of Fe_2O_{3total} and $Fe^{3+}/\Sigma Fe$ in alpine serpentinites. There is no obvious change of the Fe_2O_{3total} in serpentinites during prograde metamorphism. At the opposite, the release of Fe^{3+} requires a decrease of about 3 wt% of Fe_2O_3 in fluids to decrease the $Fe^{3+}/\Sigma Fe$ from 0.7 to 0.5.

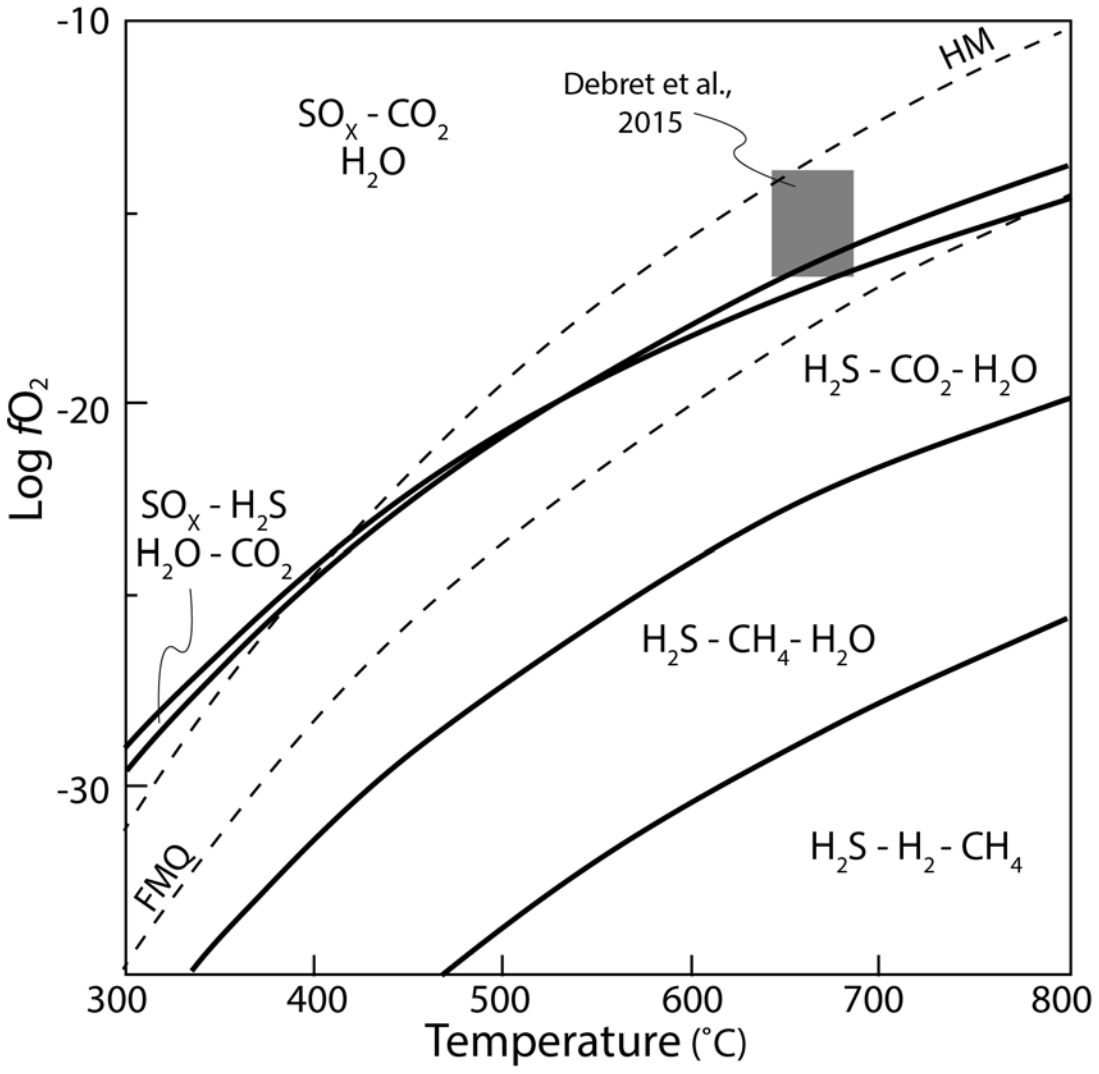

Figure DR7. Log fO_2-T diagram illustrating the redox conditions of H-S-C-O fluids at 1.5 GPa (modified after Ohmoto, 1986). The dotted lines show the fO_2-T conditions of well-known mineral buffers (HM: hematite-magnetite; FMQ: Fayalite-Magnetite-Quartz). The grey box shows the fO_2-T conditions of meta-peridotite crystallization during subduction (Debret et al., 2015). Sulfates are presented under SO_X form since the disproportionation of SO_2 can contribute to form SO, SO_3^{2-}, $S_2O_3^{2-}$ or SO_4^{2-} rich fluids (e.g. Gamo et al., 1997).

Table DR1: Iron isotope composition of studied ultramafic rocks

Sple	Serp. Mineral	Fe_2O_{3total} (wt%)	$Fe^{3+}/\Sigma Fe$	Al_2O_3/SiO_2	$\delta^{56}Fe$ (‰)*	2sd	N	$\delta^{56}Fe$ (‰)	2sd	$\delta^{57}Fe$ (‰)	2sd	N
Sligthly Serpentinized peridotite												
Mag26	-	8.3	0.13	0.05	-0.069	0.024	2	-0.100	-	-0.171	-	1
Mag33	-	8.4	-	0.06	-0.010	0.043	1	0.020	0.039	0.047	0.107	4
LZ17a	-	8.9	0.25	0.06	0.012	0.030	2	-0.020	-	-0.037	-	1
LZ19	-	8.9	0.19	0.07	0.063	0.042	4	0.035	0.037	0.029	0.034	2
LZ7	-	6.8	-	0.01	-	-		-0.133	0.046	-0.213	0.108	3
Liz-Serpentinite												
HLY102D7073	Liz	7.6**	0.64	-	-	-		-0.077	0.078	-0.109	0.132	4
HLY102D7099	Liz	7.5**	0.72	-	-0.059	0.020	2	-	-	-	-	-
HLY102D8708	Liz	4.7**	0.86	-	-	-		-0.057	0.075	-0.125	0.199	2
PS5924619	Liz	6.7**	0.72	-	-	-		0.003	0.063	0.036	0.139	8
BCh10	Liz	8.1	0.65	0.05	0.039	0.019	6	0.034	0.011	0.045	0.053	2
ICh02	Liz	7.8	0.70	0.02	-0.051	0.035	2	-0.062	0.078	-0.096	0.028	2
BCh6	Liz±Atg	7.9	0.62	0.07	0.047	0.042	4	0.006	0.070	0.003	0.102	2
RQ30	Liz±Atg	9.0	0.68	0.04	-0.098	0.020	3	-	-	-	-	-
Atg/Liz-serpentinite												
BCH9	Liz/Atg	7.9	0.56	0.08	0.080	0.013	6	0.034	-	0.059	-	1
RQ23	Liz/Atg	9.4	0.55	0.02	0.080	0.014	6	-	-	-	-	-
RQ01	Atg±Liz	7.6	0.63	0.03	0.032	0.018	6	-	-	-	-	-
MM8	Liz/Atg	9.5	0.68	0.05	0.044	0.021	3					2
MM15	Liz/Atg	7.9	0.51	0.05	0.114	0.039	4	-	-	-	-	-
MM19	Atg±Liz	8.9	0.53	0.05	0.090	0.040	3	0.115	0.095	0.125	0.064	2
MM2	Atg	8.0	0.60	0.05	0.017	0.014	6	0.006	0.012	-0.014	0.014	2
Atg-serpentinite												
LZ30	Atg	6.2	-	0.06	-	-		0.060	0.032	0.126	0.085	3
LZ14b	Atg	8.4	0.54	0.06	0.137	0.022	2	0.117	0.034	0.188	0.017	2

LZ8b	Atg	9.7	-	0.06	-	-		-0.011	0.065	-0.002	0.096	5
LZ34d	Atg	7.3	0.51	0.08	-	-		0.142	0.045	0.210	0.100	4
Vis1	Atg	8.1	0.54	0.05	0.095	0.029	2	0.129	0.072	0.174	0.215	2
Vis1F	Atg	6.1	-	0.04	-	-		0.086	0.047	0.133	0.031	4
Vis9	Atg	9.2	-	0.04	-	-		0.042	0.058	0.082	0.090	6
Atg/Ol2-serpentinite												
LZ5	Atg	8.1	-	0.05	-	-		-0.010	0.063	-0.009	0.111	4
LZ26a	Atg	5.6	-	0.06	-	-		-0.020	0.018	-0.043	0.053	2
RO1	Atg	8.1	0.53	0.07	0.016	0.025	2	-0.003	-	0.023	-	1
LZ27a	Atg	8.5	0.24	0.06	-0.035	0.018	6	-	-	-	-	-
Vis12	Atg	7.5	-	0.03	-	-		-0.054	0.038	-0.082	0.050	4
Vis5b	Atg	9.2	0.52	0.03	-	-		-0.057	0.065	-0.130	0.142	4

*Double spike values **determined by MC-ICP-MS

Table DR2: Compilation of trace element (ppm) analyses

	Mag26	Mag33	LZ17a	LZ35b	LZ19	LZ7	ICH02	BCh10	BCh6	BCh9	MM2	MM8	MM19	MM15	LZ26c	LZ30	LZ14b
Li	1.62	2.05	2.83	3.10	0.80	0.61	265.65	0.51	1.50	0.81	2.89	0.55	0.86	0.59	0.08	0.01	0.00
Sc	12.51	11.39	13.04	13.37	11.75	5.09	n.d.	9.49	9.89	11.34	10.45	11.10	11.01	11.60	12.48	11.58	11.43
V	61.12	53.24	65.53	72.08	61.76	18.78	n.d.	43.39	47.92	52.12	51.06	51.37	56.86	56.26	61.19	54.40	56.83
Cr	2650	2108	n.d.	n.d.	n.d.	n.d.	n.d.	1870	2124	1839	1849	1991	1742	2648	n.d.	n.d.	n.d.
Co	94.48	87.02	99.24	83.19	91.00	81.24	93.55	82.82	84.92	84.88	62.54	86.18	98.35	83.40	69.23	71.41	79.81
Ni	1828	1706	2109	1992	2244	2585	1811	1652	1692	1687	1693	1604	1749	1615	1201	893	1821
Cu	15.550	20.760	21.414	31.382	18.096	0.499	27.966	6.700	1.139	6.444	11.740	7.376	2.529	12.010	6.179	2.785	1.574
Zn	46.020	40.940	42.820	43.493	47.981	38.711	146.297	33.270	33.690	35.330	37.440	32.250	31.250	51.300	38.103	43.304	28.871
As	0.603	0.572	0.046	0.057	0.049	0.037	0.221	0.463	0.458	0.531	0.869	0.499	0.534	0.530	0.034	1.231	0.089
Rb	0.040	0.049	0.032	0.084	0.059	0.044	0.112	0.031	0.103	0.122	0.062	0.042	1.011	0.027	0.005	0.012	0.051
Sr	0.685	8.089	1.282	19.158	5.436	0.999	1.341	1.196	5.628	3.554	1.311	0.939	8.569	1.380	0.227	0.062	0.286
Y	1.734	1.593	2.130	3.999	3.398	0.131	0.364	1.443	2.011	2.588	1.161	1.494	2.179	1.649	1.126	0.463	0.593
Zr	0.723	0.490	1.304	7.797	4.800	0.210	0.693	0.678	3.279	2.258	0.321	0.361	3.298	0.449	0.759	0.354	0.875
Nb	0.004	0.004	0.004	0.035	0.005	0.014	0.016	0.003	0.003	0.063	0.015	0.006	0.238	0.003	0.003	0.003	0.017
Sb	0.012	0.009	0.006	0.004	0.005	0.004	0.028	0.004	0.006	0.007	0.120	0.020	0.014	0.009	0.007	0.110	0.015
Cs	0.005	0.006	0.013	0.022	0.002	0.013	0.006	0.008	0.026	0.005	0.043	0.028	0.038	0.004	0.000	0.001	0.006
Ba	0.160	0.187	0.242	0.985	0.168	0.275	7.140	0.136	0.286	0.710	0.610	0.730	15.180	1.761	b.d.l.	0.338	0.185
La	0.011	0.011	0.007	0.169	0.097	0.016	0.058	0.003	0.016	0.057	0.215	0.008	0.529	0.007	0.005	0.004	0.053
Ce	0.026	0.031	0.047	0.674	0.441	0.040	0.127	0.023	0.123	0.176	0.138	0.018	1.113	0.017	0.019	0.006	0.110
Pr	0.009	0.009	0.020	0.135	0.090	0.006	0.016	0.011	0.039	0.043	0.078	0.010	0.158	0.006	0.005	0.002	0.028
Nd	0.077	0.092	0.200	0.855	0.601	0.037	0.088	0.109	0.282	0.325	0.337	0.092	0.696	0.069	0.044	0.013	0.165
Sm	0.067	0.075	0.123	0.345	0.251	0.012	0.038	0.075	0.146	0.178	0.112	0.073	0.206	0.069	0.025	0.008	0.063
Eu	0.033	0.032	0.057	0.154	0.110	0.007	0.019	0.035	0.058	0.079	0.042	0.033	0.096	0.048	0.009	0.007	0.009
Gd	0.168	0.167	0.255	0.594	0.458	0.016	0.056	0.144	0.244	0.311	0.158	0.165	0.287	0.156	0.059	0.024	0.104
Tb	0.037	0.034	0.050	0.104	0.083	0.003	0.008	0.032	0.048	0.060	0.032	0.034	0.054	0.036	0.012	0.005	0.019
Dy	0.280	0.266	0.388	0.761	0.616	0.021	0.055	0.229	0.333	0.442	0.219	0.261	0.391	0.270	0.113	0.050	0.136
Ho	0.068	0.064	0.088	0.164	0.135	0.005	0.011	0.056	0.075	0.099	0.048	0.061	0.088	0.065	0.032	0.015	0.029
Er	0.216	0.197	0.256	0.458	0.385	0.015	0.031	0.177	0.230	0.295	0.140	0.179	0.259	0.208	0.124	0.060	0.081
Tm	0.035	0.032	0.039	0.067	0.057	0.003	0.005	0.028	0.036	0.045	0.022	0.029	0.040	0.032	0.024	0.013	0.013
Yb	0.243	0.224	0.263	0.432	0.372	0.023	0.034	0.205	0.250	0.309	0.150	0.203	0.289	0.229	0.182	0.111	0.088
Lu	0.039	0.038	0.046	0.072	0.062	0.006	0.006	0.032	0.037	0.050	0.021	0.031	0.047	0.037	0.035	0.022	0.015
Hf	0.049	0.039	0.067	0.232	0.156	0.006	0.033	0.045	0.133	0.110	0.025	0.037	0.121	0.036	0.046	0.030	0.040
Ta	b.d.l.	b.d.l.	0.0004	0.0037	0.0013	0.0007	0.0009	b.d.l.	b.d.l.	b.d.l.	b.d.l.	b.d.l.	b.d.l.	b.d.l.	0.0002	0.0002	0.0003
Pb	0.134	0.124	b.d.l.	b.d.l.	0.060	b.d.l.	4.988	0.138	0.173	0.214	0.180	0.291	0.923	0.115	b.d.l.	0.112	0.141

Th	0.005	0.005	0.001	0.005	0.001	0.001	0.011	0.001	0.002	0.011	0.001	0.002	0.127	0.001	b.d.l.	0.001	0.002
U	0.0019	0.0177	0.0004	0.0018	0.0004	0.0007	0.0088	0.0004	0.0009	0.0021	0.0020	0.0005	0.0406	0.0032	0.0003	0.0004	0.0060

n.d.: non detected, b.d.l.: below detection limit; data are from Debret et al. (2013), Lafay et al. (2013) and this study

LZ8b	LZ5	LZ26a	RO1	LZ27A	LZ34d	Vis1	Vis1F	Vis9	Vis12	Vis5b	RQ30	RQ23	RQ01
0.05	2.00	0.03	0.16	1.14	0.45	0.14	0.01	0.07	0.19	0.02	2109.91	483.39	49.51
9.18	8.90	11.23	12.68	7.87	10.65	9.85	12.15	5.82	12.13	6.89	n.d.	n.d.	n.d.
58.61	47.02	50.87	65.65	37.48	57.29	59.68	62.93	31.79	48.10	27.57	n.d.	n.d.	n.d.
n.d.	n.d.	n.d.	n.d.	n.d.	n.d.	n.d.	n.d.	n.d.	n.d.	n.d.	n.d.	n.d.	n.d.
93.93	95.77	76.13	97.86	97.28	85.77	94.11	80.68	55.28	95.19	61.96	93.56	98.05	82.89
1283	2245	1154	2246	2126	2106	2266	1910	1143	1943	1212	1819	2021	1083
11.577	11.290	7.492	9.372	4.116	6.342	13.873	7.374	3.580	6.771	4.468	14.448	43.427	6.560
47.145	38.504	37.225	50.157	35.278	36.180	29.457	37.150	24.331	39.427	22.231	37.000	56.700	44.856
0.041	0.057	0.043	0.127	0.043	0.053	0.061	0.062	0.052	0.067	0.026	0.143	0.898	3.974
0.029	0.056	0.017	0.104	0.055	0.077	0.011	0.013	0.021	0.010	0.003	0.154	0.199	0.069
0.537	6.083	0.152	1.821	7.411	9.986	0.530	0.146	0.174	2.516	0.223	4.606	2.040	0.297
1.522	1.896	1.203	2.455	1.711	3.008	1.822	1.055	0.347	0.982	0.260	1.302	0.571	0.494
2.006	3.456	0.980	2.629	2.621	4.470	1.041	0.062	0.066	0.700	0.204	0.404	1.248	0.074
0.016	0.003	0.006	0.027	0.016	0.027	0.009	0.004	0.013	0.007	0.005	0.011	0.023	0.012
0.008	0.010	0.004	0.012	0.004	0.008	0.007	0.009	b.d.l.	0.010	0.014	0.014	0.129	0.995
0.009	0.018	0.001	0.062	0.009	0.024	0.000	0.000	0.005	0.001	0.000	0.246	0.647	0.008
0.804	0.724	b.d.l.	8.886	0.204	0.364	0.223	0.135	0.331	0.695	b.d.l.	3.024	1.085	0.895
0.025	0.055	0.028	0.050	0.086	0.127	0.047	0.019	0.013	0.088	0.014	0.036	0.103	0.056
0.098	0.255	0.089	0.201	0.340	0.500	0.124	0.024	0.043	0.290	0.027	0.127	0.208	0.130
0.021	0.056	0.016	0.053	0.064	0.099	0.023	0.003	0.007	0.045	0.003	0.025	0.028	0.014
0.151	0.369	0.109	0.390	0.392	0.641	0.152	0.017	0.045	0.230	0.016	0.157	0.134	0.063
0.079	0.157	0.052	0.186	0.153	0.256	0.072	0.013	0.016	0.078	0.008	0.062	0.038	0.016
0.020	0.062	0.002	0.091	0.075	0.105	0.009	0.003	0.003	0.025	0.003	0.026	0.026	0.008
0.175	0.292	0.123	0.353	0.249	0.437	0.165	0.051	0.035	0.125	0.022	0.116	0.056	0.035
0.036	0.051	0.024	0.064	0.044	0.077	0.032	0.014	0.007	0.023	0.005	0.023	0.010	0.008
0.296	0.379	0.194	0.484	0.325	0.566	0.274	0.142	0.054	0.176	0.041	0.175	0.073	0.069
0.068	0.082	0.046	0.105	0.071	0.121	0.065	0.039	0.014	0.040	0.010	0.041	0.017	0.017
0.212	0.228	0.136	0.303	0.207	0.340	0.194	0.135	0.047	0.121	0.036	0.125	0.054	0.056
0.034	0.035	0.022	0.044	0.031	0.051	0.029	0.024	0.008	0.018	0.007	0.019	0.009	0.009
0.225	0.221	0.150	0.286	0.208	0.330	0.173	0.171	0.060	0.121	0.053	0.132	0.074	0.071
0.039	0.039	0.026	0.049	0.036	0.057	0.026	0.030	0.011	0.021	0.011	0.025	0.015	0.012
0.074	0.108	0.043	0.108	0.083	0.145	0.028	0.008	0.004	0.026	0.007	0.019	0.039	0.006
0.0012	0.0007	0.0004	0.0019	0.0013	0.0028	0.0006	0.0001	0.0007	0.0005	0.0003	0.0008	0.0018	0.0009
b.d.l.	b.d.l.	b.d.l.	0.139	b.d.l.	b.d.l.	0.090	0.063	b.d.l.	0.067	b.d.l.	b.d.l.	1.541	1.071

0.002	0.001	0.001	0.004	0.002	0.003	0.003	0.001	0.001	0.003	0.001	0.001	0.005	0.014
0.0007	0.0014	0.0008	0.0011	0.0009	0.0010	0.0008	0.0006	0.0009	0.0012	0.0003	b.d.l.	0.0036	0.0030

REFERENCES CITED:

Andreani, M., Muñoz, M., Marcaillou, C., and Delacour, A., 2013, μXANES study of iron redox state in serpentine during oceanic serpentinization: Lithos, v. 178, p. 70-83.

Bodinier, J.L., and Godard, M., 2013, Orogenic, Ophiolitic, and Abyssal Peridotites, *in* R.W. Carlson, ed., Mantle and Core: Treatise on Geochemistry, v. 2, p. 103-151.

Caby, R., 1995, Plastic deformations of gabbros in a slow-spreading mesozoic Ridges: example of the Montgenèvre Ophiolite, Western Alps. In: Vissers, R.L.M., Nicolas, A. (Eds.), Proc. Workshop on Mantle and Lower Crust Exposed in Oceanic Ridges and in Ophiolites. Kluwer, Dordrecht, pp. 123–145.

Debret, B., Andreani, M., Godard, M., Nicollet, C., Schwartz, S., and Lafay, R., 2013, Trace element behavior during serpentinization/deserpentinization of an eclogitized oceanic lithosphere: a LA-ICPMS study of the Lanzo ultramafic massif (Western Alps): Chemical Geology, v. 357, p. 117-133.

Debret, B., Andreani, M., Muñoz, M., Bolfan-Casanova, N., Carlut, J., Nicollet, C., Schwartz, S., and Trcera, N., 2014, Evolution of Fe redox state in serpentine during subduction: Earth and Planetary Science Letters, v. 400, p. 206-218.

Debret, B., Bolfan-Casanova, N., Padrón‐Navarta, J.A., Martin‐Hernandez, F., Andreani, M., Garrido, C., López Sanchez‐Vizcaino, V., Gomez‐Pugnaire, M.T., Muñoz, M., and Trcera, N., 2015, Redox state of iron during high pressure serpentinite dehydration: Contribution to Mineralogy and Petrology, v. 169:36.

Gamo, T., Okamura, K., Charlou, J.L., Urabe, T., Auzende, J.M., Ishibashi, J., Shitashima, K. and H. Chiba, 1997, Acidic and sulfate-rich hydrothermal fluids from the Manus back-arc basin, Papua New Guinea: Geology, v. 25 , p. 139-142.

Govindaraju, K., 1994, Compilation of working values and sample description for 383 geostandards: Geostandards Newsletter, v. 18, p. 1-158.

Hibbert, K.E.J., Williams, H.M., Kerr, A.C., Puchtel, I.S., 2012. Iron isotopes in an-cient and modern komatiites: evidence in support of an oxidised mantle from Archean to present: Earth and Planetary Science Letters, v. 321, p. 198–207.

Lafay, R., Deschamps, F., Schwartz, S., Guillot, S., Godard, M., Debret, B., and Nicollet, C., 2013, High-pressure serpentinites, a trap-and-release system controlled by metamorphic conditions: example from the Piedmont zone of the western Alps: Chemical Geology, v. 343, p. 38–54.

Mével, C., Caby, R. and Kienast, J.R., 1978, Amphibolite facies conditions in oceanic crust: example of amphibolitized flaser gabbros and amphibolites from the Chenaillet ophiolite massif (Hautes Alpes, France): Earth and Planetary Science Letters, v. 39, p. 98–108.

Millet, M.A. Baker, J.A., and Payne, C.E., 2012, Ultra-precise stable Fe isotope measurements by high resolution multiple-collector inductively coupled plasma mass spectrometry with a 57 Fe–58 Fe double spike: Chemical Geology, v. 304, p. 18–25.

Ohmoto, H, 1986, Stable isotope geochemistry of ore deposits in J.W Valley (Ed.), et al., Stable Isotopes in High Temperature Geological Processes: Reviews in Mineralogy, v. 16, p. 491–559

Paulick, H., Bach, W., Godard, M., De Hoog, J.C.M., Suhr, G. and Harvey, J., 2006, Geochemistry of abyssal peridotites (Mid-Atlantic Ridge, 15°20′N, ODP Leg 209): implications for fluid/rock interaction in slow spreading environments. Chemical Geology, v. 234, p. 179–210.

Pelletier, L. and Müntener, O., 2006, High-pressure metamorphism of the Lanzo peridotite and its oceanic cover, and some consequences for the Sezia–Lanzo zone (northwestern Italian Alps): Lithos, v. 90, p. 111–130.

Rouméjon, S., Cannat, M., Agrinier, P., Godard, M., and Andreani, M. Serpentinization and Fluid Pathways in Tectonically Exhumed Peridotites from the Southwest Indian Ridge (62–65°E): Journal of Petrology, doi:10.1093/petrology/egv014.

Schwartz, S., Allemand, P. and Guillot, S., 2001, Numerical model of the effect of ser- pentinites on the exhumation of eclogitic rocks: insights from the Monviso ophiolitic massif (Western Alps): Tectonophysics, v. 342, p. 193–206.

Schwartz, S., Guillot, S., Reynard, B., Lafay, R., Debret, B., Nicollet, C., Lanari, P. and Auzende, A.L., 2013, Pressure–temperature estimates of the lizardite/antigorite transition in high pressure serpentinites, Lithos, v. 178, p. 197–210.

Tricart, P. and Schwartz, S., 2006, A north–south section across the Queyras Schistes lustrés (Piedmont zone, Western Alps): syncollision refolding of a subduction wedge: Eclogae Geologicae Helvetiae, v. 99, p. 429–442.

Vitale Brovarone, A., Beyssac, O., Malavieille, J., Molli, G., Beltrando, M. and Compagnoni, R., 2013, Stacking and metamorphism of continuous segments of subducted lithosphere in a high-pressure wedge: the example of Alpine Corsica (France): Earth-Science Review, v. 116, 35–56.

Weyer, S., and Ionov, D.A., 2007, Partial melting and melt percolation in the mantle: the message from Fe isotopes. Earth and Planetary Science Letters, v. 259, p. 119–133.

Williams, H.M., Peslier, A.H., McCammon, C., Halliday, A.N., Levasseur, S., Teutsch, N., and Burg, J.P., 2005, Systematic iron isotope variations in mantle rocks and minerals: the effects of partial melting and oxygen fugacity. Earth and Planetary Science Letters, v. 235, p. 435–452.

Williams, H.M., and Bizimis, M., 2014. Iron isotope tracing of mantle heterogeneity within the source regions of oceanic basalts. Earth and Planetary Science Letters, v. 404, p. 396-407.